A Biradical Balancing Act: Redox Amphoterism in a Diindenoanthracene Derivative Results from Quinoidal Acceptor and Aromatic Donor Motifs

A Biradical Balancing Act: Redox Amphoterism in a Diindenoanthracene Derivative Results from Quinoidal Acceptor and Aromatic Donor Motifs

Gabriel E. Rudebusch,[†] Guzma´n L. Espejo,[‡] Jose´ L. Zafra,[‡] Miriam Pen˜a-Alvarez,[‡] Sarah N. Spisak,[§] Kotaro Fukuda,[∥] Zheng Wei,[§] Masayoshi Nakano,*[,∥] Marina A. Petrukhina,*[,§] Juan Casado,*[,‡] and Michael M. Haley*[,†]

[†]Department of Chemistry & Biochemistry and the Materials Science Institute, University of Oregon, Eugene, Oregon 97403-1253, United States

[‡]Department of Physical Chemistry, University of Malaga, Campus de Teatinos s/n 229071 Malaga, Spain

[§]Department of Chemistry, University at Albany, State University of New York, Albany, New York 12222-0100, United States

[∥]Department of Materials Engineering Science, Graduate School of Engineering Science, Osaka University, Toyonaka, Osaka 560-8531, Japan

Supporting Information Placeholder

ABSTRACT: The reduced and oxidized states of an open-shell diindeno[*b*,*i*]anthracene (**DIAn**) derivative have been investigated by experimental and theoretical techniques. As a result of significant biradical character and the ability of cyclopenta-fused scaffolds to stabilize both positive and negative charges, **DIAn** exhibits rich redox chemistry with four observable and isolable charged states. Structural and electronic properties of the **DIAn** system are brought to light by UV-vis-NIR and Raman spectroelectrochemical measurements. Aromatization of the cyclopenta-fused scaffold upon successive single electron injections is revealed through single-crystal X-ray diffraction of radical anion and dianion salts. We present a rare case where the pseudo-aromatic/quinoidal ground state of a neutral biradical PCH leads to a stable cascade of five redox states. Our detailed investigation of the transformation of molecular structure along all four redox events provides a clearer understanding of the nature of charge carriers in ambipolar OFETs.

Introduction

Polycyclic hydrocarbons (PCHs) very often exhibit rich redox chemistry in addition to unique electronic and optical properties. The exploration of the charge distribution, magnetism, electronic structure and solid-state morphology of redox-active PCHs are well-engrained areas of physical organic chemistry.[1–5] The practical application of redox active PCHs and related materials has seen considerable growth in recent years as the limits of traditional inorganic-based systems are becoming evident.[6–8] A related field experiencing a burst of activity involves the synthesis and characterization of PCHs with biradical character.[9–12] Typically, high levels of reactivity are associated with the pair of loosely correlated electrons. As a consequence of new synthetic approaches and improved spectroscopic techniques, numerous stable biradical PCHs have been reported in the last decade.[10,11] The molecules exhibit many favorable properties, including redox amphoterism, strong absorption in the visible spectrum, small frontier orbital energy gaps (<1.5 eV), large second hyperpolarizabilities, and the opportunity of modulating spin-state through thermally accessible triplet states.[13–15]

Generally, most of these π–conjugated systems are excellent electron-donors, easily stabilizing positive charges, and, proportionally, only a few are good electron-acceptors able to stabilize negative charges. This originates from the abundance of p-type semiconductors and the recent increase of n-type semiconductors.[16] In this context, ambipolar semiconductors represent "water in the desert" given the inherent difficulty of the same π–conjugated structure to equally accommodate charge carriers of either sign.[17,18] The connection between ambipolar semiconductor behavior and molecular redox amphoterism is well-established and this has been discovered in PCHs with moderate biradical character.[10] The electronic configuration of a biradical PCH is illustrated by the relatively high-lying highest occupied molecular orbital (HOMO) energy and low-lying lowest unoccupied molecular orbital (LUMO) energy, which in concert, provides the thermodynamic driving force for reversible injection and extraction of electrons.

The application of redox-active biradical PCHs is only recently coming into the fold of organic electronics and spintronics. Organic radical batteries based on stable nitroxyl radical polymers[19] or trioxotriangulene systems[20] are attractive alternatives to the current generation of metal ion batteries given their fast charging speed, cycling stability and environmental sustainability. Information storage using redox-active organic compounds as memory elements is another potentially fruit-

ful area of research as a single molecule could, in principle, represent the physically smallest bit of information.[21] The prospects of controlling molecular spin information by varying redox states is an appealing aspect of redox responsive PCHs. A remarkable example of a viologen-containing homocatenane with six accessible and air-stable charged states was recently reported.[22] The interlocked molecule was shown to switch between diamagnetic and paramagnetic forms as a function of oxidation state. The ability to stabilize both negative and positive charges, as well as metal-like electron delocalization in the solid-state, has been exploited in ambipolar OFETs based on redox amphoteric small molecules.[23,24] Koike and co-authors demonstrated highly coherent band transport in thin films based on an indacenodiphenalene derivative. The excellent performance of the OFETs is likely due to the intimate π-π contacts and multi-center bonding between molecules.[25]

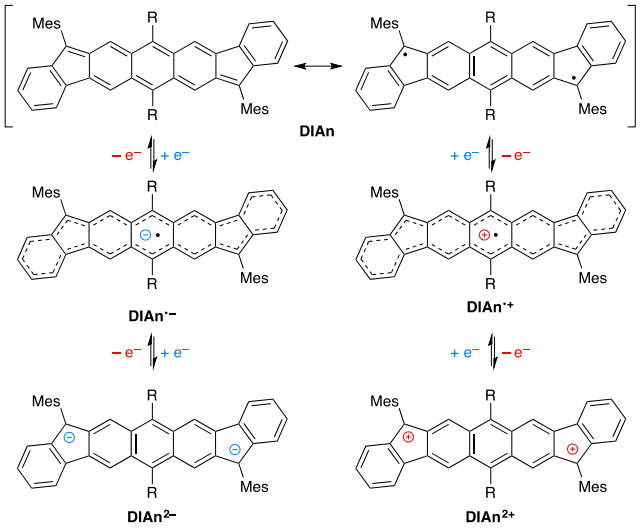

Figure 1. Redox processes of **DIAn**: the ground state is a resonance hybrid of quinoidal (acceptor, top left) and aromatic (donor, top right) structures. R = (triisopropylsilyl)ethynyl.

We recently reported the diindeno[*b*,*i*]anthracene derivative **DIAn** as an oxygen- and temperature-stable singlet biradical compound (Figure 1).[26] The ground-state is best described as a balance of quinoidal closed-shell and aromatic open-shell resonance structures. In connection with a frontier orbital energy gap of 1.45 eV and a moderate biradical character index[27] of y = 0.62, **DIAn** exhibits two reversible one-electron reductions and two reversible one-electron oxidations as disclosed in the cyclic voltammetry (CV) experiment (Figure 2). The marked symmetry between all four redox waves, indicating similar electro-kinetic parameters, and good resolution between each wave (ΔE_{red} = 0.39 V, ΔE_{ox} = 0.53 V), led to the hypothesis that each charged species (Figure 1) could be accessed and characterized independently. Indeed, the stability and efficient gram-scale synthesis of **DIAn** facilitated further experiments and exploration of this new open-shell PCH scaffold. While redox-active biradical PCHs based on a large acene cores are known,[28–30] this study represents a thorough experimental and theoretical investigation of the reduced and oxidized states of **DIAn** and the transformation of molecular structure along all four redox events. Our results provide a clearer understanding of the nature of charge carriers in ambipolar OFETs and serve as a platform for further modification of the diindenoacene family.

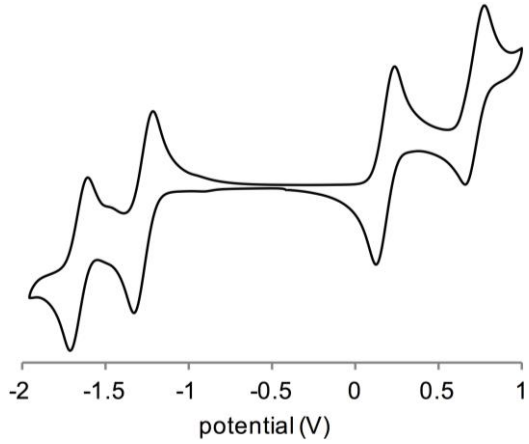

Figure 2. Cyclic voltammogram of **DIAn** in CH_2Cl_2 vs. ferrocene/ferrocenium.

Results and Discussion

UV-Vis-NIR absorption Spectroelectrochemistry. The redox processes examined in solution cyclic voltammetry were studied by UV-vis-NIR spectroelectrochemistry. In the anodic branch (Figure 3, top), the first one-electron oxidation gives rise to a spectrum with two main bands at 867 nm and 1945 nm. Interestingly, the 867 nm peak is also observed when **DIAn** is heated to 135 °C in 1,1,2,2-tetrachloroethane (Figure S1 in the SI) with the intensity showing a decrease upon cooling to 25 °C. This could be due to a reversible redox process with oxygen or self-doping in which two sandwiched molecules undergo charge exchange giving rise to a charge transfer complex. Nonetheless, the reversibility of the reaction reveals the robustness of the material versus degradative oxidation. The low energy absorbance (1945 nm, 0.65 eV) is typical of a PCH radical cation and can be assigned to a SOMO→LUMO singly excited transition[31] while the 867 nm absorbance has major contributions from the HOMO→SOMO transition of **DIAn**$^{\bullet+}$ (See SI). Increasing the anodic potential further yields two new bands centered at 744 nm and 1026 nm, presumably due to **DIAn**$^{2+}$. The low energy absorption can be assigned to a weak HOMO→LUMO transition.

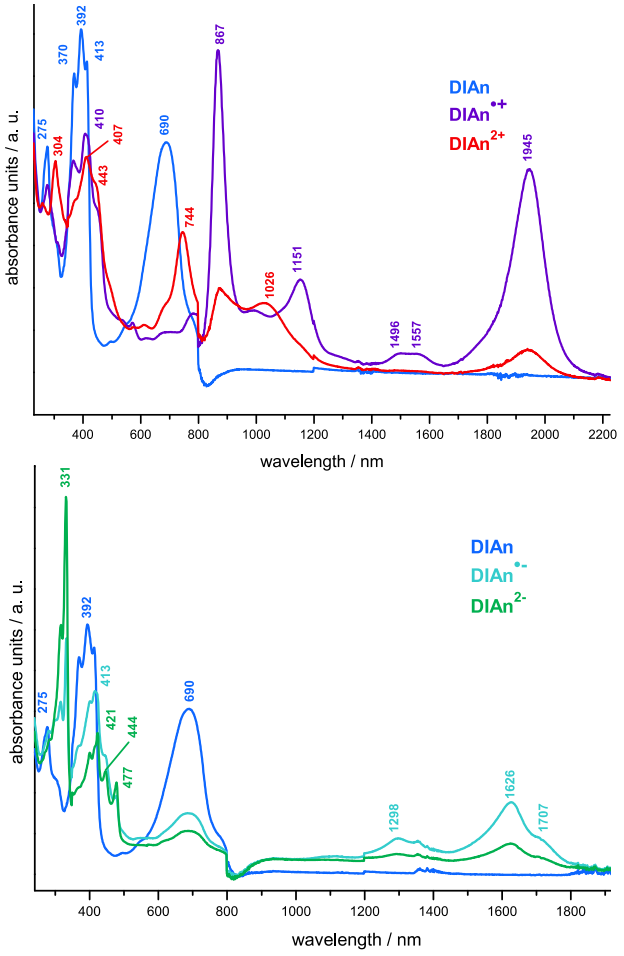

Figure 3. The oxidation (top) and reduction (bottom) of **DIAn** followed by UV-vis-NIR spectroelectrochemistry. Conditions: CH_2Cl_2, 0.1 M [*n*-Bu_4N][PF_6].

The one-electron reduction process shows disappearance of the neutral absorption at 690 nm and the emergence of two groups of bands centered at 1600–1700 nm and at 400 nm (Figure 3, bottom). The low energy (~0.75 eV) absorbance can be attributed to a HOMO→SOMO singly excited transition of **DIAn**$^{\bullet-}$ (See SI). Again, this is typical of a quinoidal PCH radical anion where the skeletal backbone has regained partial aromaticity.[32,33] With increasing cathodic potential, a clear progression to **DIAn**$^{2-}$ is observed with new peaks at 330 nm and typical rigid acene absorbance from 440 to 470 nm. These anthracene-like vibronic features are in good agreement with those of the dihydro precursor of **DIAn** that also contains an aromatic anthracene core appended by saturated indeno fragments (Figure S4).[26] According to the optimized structures for the two singly **DIAn**$^{\bullet+}$ and **DIAn**$^{\bullet-}$ redox species, one would expect further similitude between their absorption spectra, which actually differ by 0.1 eV in the low-lying absorption energy bands. This slight difference indicates the easier charge delocalization of a hole (among many π electrons) than an excess electron in the similar π–electron cloud (i.e., the 0.1 eV energy might account for the extra energy to overcome extra π–repulsion within excitation). This effect is more significant in the **DIAn**$^{2-}$/**DIAn**$^{2+}$ pair due the increasing number of holes/electrons. In parallel with the spectroelectrochemical experiment, chemical reduction with K metal and oxidation with $NOBF_4$ gave analogous absorption spectra (Figures S2 and S3), thus confirming the assignment of the UV-vis-NIR electrolysis experiments.

Vibrational Raman Spectroelectrochemistry. Raman spectroelectrochemical measurements were carried out to investigate the change in molecular structure with each redox event. The Raman spectra of **DIAn** during electrolysis are shown in Figure 4. We focus our analysis to the 1600–1550 cm^{-1} spectral range where the structurally relevant C=C stretching vibrations of PCH backbones, ν(C=C), appear. The Raman spectrum of neutral **DIAn** shows a band at 1590 cm^{-1} due to the characteristic ν(C=C) stretching mode of the pseudo-aromatic biradical anthracene structure (Figure 4a). One electron oxidation produces **DIAn**$^{\bullet+}$ with a pair of bands at 1587 and 1581 cm^{-1}. Interestingly, the Raman spectrum upon one-electron reduction to **DIAn**$^{\bullet-}$ is also characterized by a band at 1580 cm^{-1}. After the second one-electron oxidation to **DIAn**$^{2+}$, the spectrum is simplified to a single band at 1580 cm^{-1}. In the cathodic branch, a second one-electron reduction to **DIAn**$^{2-}$ again yields a similar Raman spectrum with a single band at 1582 cm^{-1}. What is significant among the different spectra is that either redox process results in Raman dispersions with main skeletal ν(C=C) bands appearing within a small range of frequencies; there is large vibrational spectroscopic resemblance revealing the structural similitudes between the doubly charged species independent of sign. This evidence suggests that the ground electronic delocalization of holes/electrons in the redox species is similar in anion/cation and dianion/dication couples in analogy with the similitudes found in the UV-Vis-NIR absorption spectra.

We have previously assigned the 1580 cm^{-1} band as the characteristic feature of the triplet excited state of neutral **DIAn** resulting from the gain of aromatic character in this thermally accessible high spin state; therefore, the appearance of ν(C=C) bands in the charged species near 1580 cm^{-1} is an indicator of the recovery of aromaticity in the anthracene core. It can be inferred that the accumulation of aromatic character during redox events is the most efficient mode of stabilizing charges of different sign. From a structural viewpoint, this can be an explanation for the mirror-like reduction and oxidation events in the CV experiment. Further, the ability to stabilize both radical anions and cations has implications in describing the microscopic charge carriers and ambipolar charge transport properties previously shown in OFETs fabricated from **DIAn**.[26]

This ability of the neutral biradical **DIAn** to access this “aromatic transformation” under different stimuli

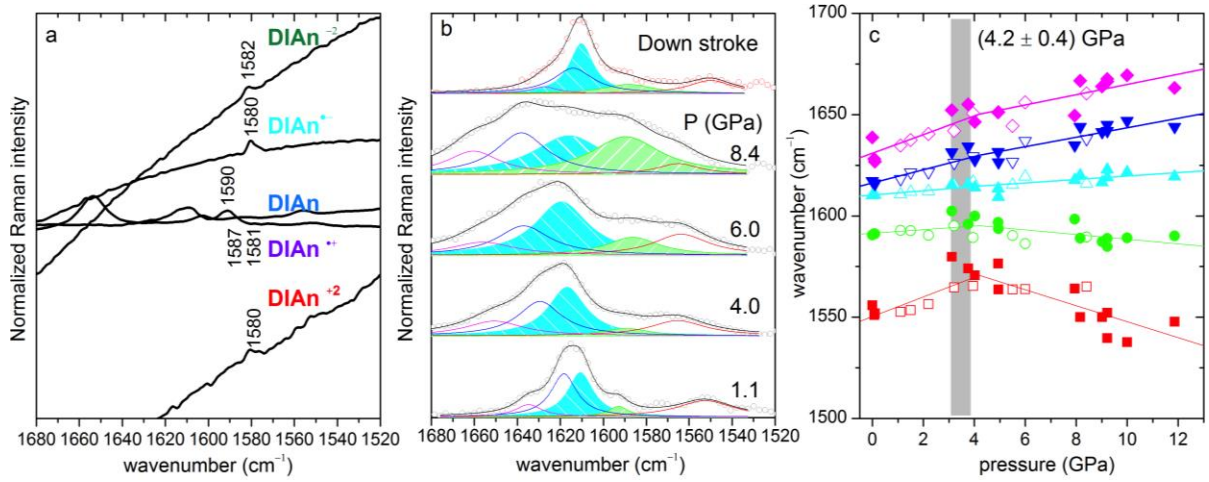

Figure 4. (a) Raman spectroelectrochemical experiment of **DIAn** excited at 785 nm. Neutral spectrum is taken at 633 nm. Conditions: 10^{-1} M with 0.1 M [*n*-Bu_4N][PF_6] in CH_2Cl_2. (b) Raman spectrum at selected pressures measured with a laser of 532 nm in the 1680-1520 cm^{-1} region. The spectra have been fitted to five contributions, which at room conditions are at: 1630, 1615, 1610, 1580, and 1550 cm^{-1}, in red, dark blue, filled cyan, filled green and red, respectively. At room temperature the 1615-1610 cm^{-1} contributions are the most intense, corresponding to ν(C=C) of the quinoidal hybrid, while the 1580 cm^{-1} band that gains intensity with increasing stress corresponds to the ν(C=C) of an anthracene-like aromatic in the **DIAn** center. (c) Raman shift pressure evolution of the contributions fitted as in Figure 4b from experimental Raman spectra taken with 633 and 532 nm, filled and empty symbols respectively. Each color corresponds to the fitted contribution. Vertical grey regions correspond to the pressures of interception between each linear trend.

(redox, heating, etc.) has also been explored under mechanical stress by applying high pressure to the solid at room temperature. The variable pressure experiment was followed by Raman spectroscopy and the results are shown in Figures 4b and 4c. The main Raman band under 532 nm laser excitation appears at 1615 cm^{-1} with a shoulder at1610 cm^{-1} and a set of weak bands 1630, 1580 and 1550 cm^{-1}. Under external pressure of 8.4 GPa, the set of weak bands are intensified with respect to the strongest band at 1610 cm^{-1} at normal pressure; however, within these new bands there is an accentuation of the 1581 cm^{-1} feature that reaches the intensity of the 1610 cm^{-1} band (see deconvoluted spectra in Figure 4). As shown in Figure S11, in the 1200-1300 cm^{-1} spectral region, there is a couple of peaks which are also altered by pressure as shown by their relative intensities at room and high applied pressure (See SI). Given the distinct response of the 1650-1550 cm^{-1} covalent molecular vibration bands to pressure (see Figure 4c) and that the low wavenumber crystal-phonon Raman region scarcely changes in the experiment (the unit cell structure thus should scarcely change in the experiment) are arguments in support of the induction of molecular levels changes upon pressure. In the ν(C=C) frequency region again the 1580 cm^{-1} band has a main presence in the spectrum, which according to the assignment above should arise from a gaining of anthracene-like aromatic character in the **DIAn** center. We can speculate that, under high pressure, the cofacial π–π arrangement of the **DIAn** molecules allows allows: (i) self-exchange of electrons giving rise to a kind of charge-transfer complex; (ii) since the molecules get closer at high pressure and given the head-to-tail π–contact in the unit cell between stacked molecules, the formation of strained long CC bond between radicals in vicinal molecules might induce the gaining of core aromaticity; and (iii) heating of the sample due to adiabatic compression should be ruled out as a source of triplet extra-population given that simultaneously the singlet-triplet gap might be increased due to enhanced intermolecular interactions. Summing up, these several situations in the pressure experiment highlight again the versatile response of **DIAn** due to its biradical character in response to molecular compression.

Solid-State Structures of Reduced DIAn Species. To gain insight into the structural changes upon one and two electron reductions, we sought to prepare and characterize salts of the radical anion and dianion in the solid-state. Brief exposure of the deep violet THF solution of **DIAn** to K metal in the presence of 18-crown-6 ether provided the solvent-separated radical anion salt **1** (Scheme 1) as dark brown plates. An X-ray diffraction study showed the **DIAn**$^{\bullet-}$ anion is centrosymmetric and planar; RMS deviation through an average plane drawn through the core is calculated to be 0.05 Å. Longer exposure to K metal provided the dianion **2** crystallized from THF/hexanes as red-brown plates. The **DIAn**$^{2-}$ core was found to be centrosymmetric and planar with a RMS deviation of 0.09 Å. Interestingly, the outer benzenoid rings are canted ca. 10° from the central anthracene ring towards the K^+ ion. Using similar experimental conditions, but with diglyme in place of 18-crown-6 ether and the inclusion of diglyme, the contact-ion pair product **3** was obtained as orange-brown plates.

Scheme 1. Synthesis of Radical Anion (1) and Dianion Salts (2,3) of DIAn by Potassium-Induced Reduction[a,b]

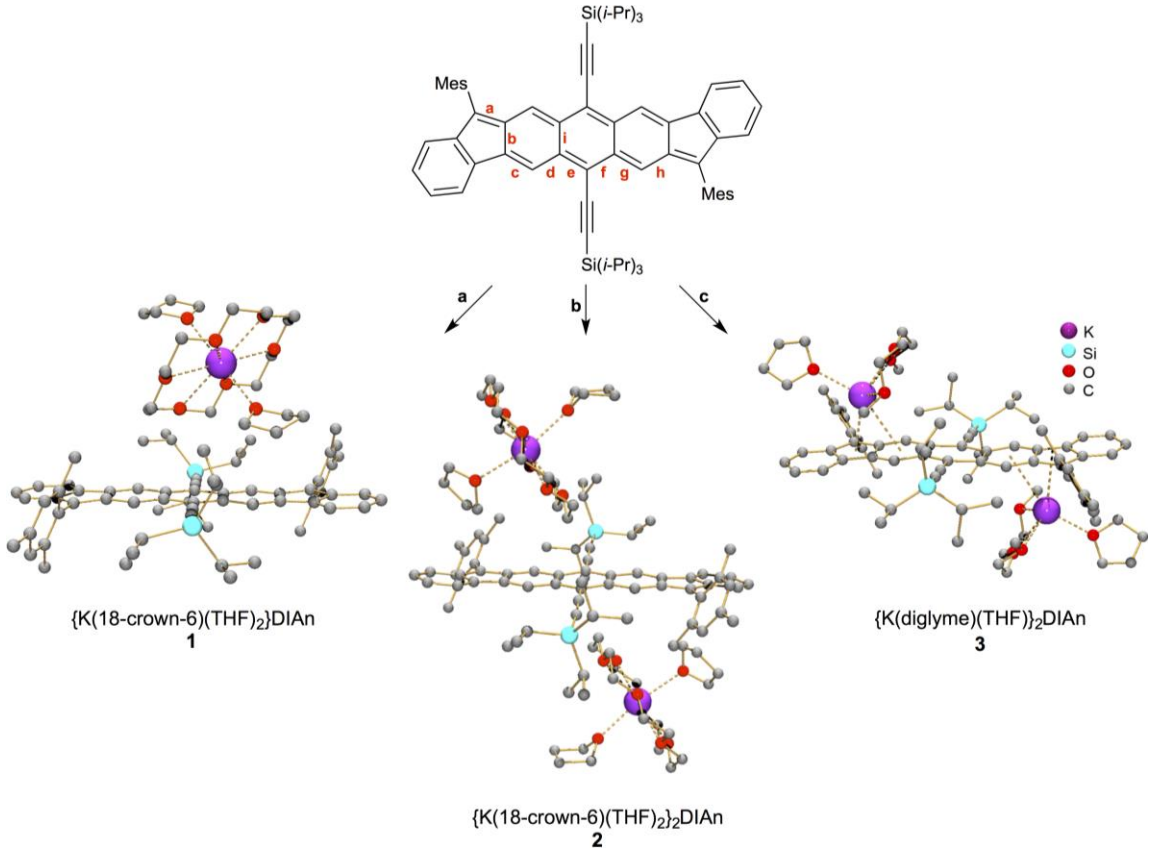

[a]Reaction conditions: (a) K, 18-crown-6, THF, 10 min; (b) K, 18-crown-6, THF, 2 h; (c) K, THF, 10 h, then diglyme/hexanes layering. [b]All H atoms in the ball-and-stick x-ray structure models of **1**-**3** omitted for clarity.

The $[K(diglyme)(THF)]^+$ ions are disordered over two positions with short K•••π-contacts of 2.91 Å (η^5) and longer ones of 3.26 (η^6) (Figure S9). In **3**, the **DIAn**$^{2-}$ core is severely distorted from planarity. Notably, **1** and **2** lack metal ion–π interactions; the $[K(18\text{-crown-}6)(THF)_2]^+$ cations are located 5.67 Å (**1**) and 6.24 Å (**2**) from the polycyclic core. This permits meaningful comparison of bond distances between the neutral ligand and "naked" reduced species.[34] Analysis of the bond distances of the non-contact ion pair products **1** and **2** reveals aromatization of the anthracene core (Figure 5). In the first reduction event, bonds b, d, f, h, and i show an average contraction of 0.017 Å. These bonds were previously ascribed partial single bond character in neutral **DIAn**. Double bonds c, e and g throughout the core remain unaffected. The structure of **1** preserves the bond distance alternation of the neutral ligand, but, as a result of an electron in a previously non-bonding orbital, there is contraction of bond distances in the core.[35,36] The $[K(18\text{-crown-}6)(THF)_2]^+$ ion is slipped by just 1.21 Å from the **DIAn**$^{\bullet-}$ centroid, indicating delocalization of the free electron (Figure 1). The next single-electron reduction to dianion **2** shows the homogenization of central bonds d, e, f, and g to 1.420 (± 0.005) Å, a value indicative of an anthracene-like structure. In fact, comparison of the bond length in **2** to the structural data of a similar saturated system gives excellent agreement (Figure S10). From the solid-state structure of **1** we observe that the first reduction results in contracted bond distances but overall retention of the quinoidal bonding pattern. The second reduction towards **2** completes the aromatization of the anthracene core. Considering the η^5-coordination of K in the contact-ion pair **3**, we can infer that the negative charges are predominantly localized on the five-membered rings giving two cyclopentadienyl-like anions that straddle the central anthracene (Figure 1).

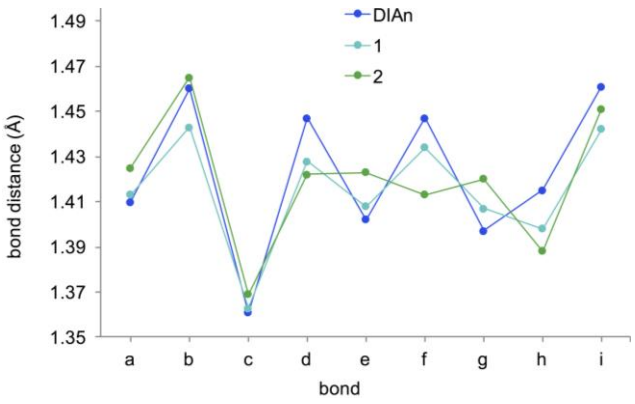

Figure 5. Single-crystal X-ray diffraction studies of neutral **DIAn** (blue), radical anion (**1**, teal) and dianion (**2**, green) discloses aromatization of the core upon reduction. See bond lettering in Scheme 1.

Computational Assessment. Quantum chemical calculations were carried out to further scrutinize the neutral, reduced and oxidized states of **DIAn**. For computational ease, the Si(*i*-Pr)$_3$ and mesityl groups in **DIAn** were simplified to SiMe$_3$ and 2,6-dimethylphenyl, respectively. The geometry optimization of the neutral state is carried out using the RB3LYP/6-311G* method, which has been confirmed to well reproduce the X-ray crystallographic data and the simplified optimized geometry at higher level of theory, the spin-flip TD-DFT method.[26] On the other hand, for the geometry optimization of the singly reduced and oxidized states, UB3LYP/6-311G* level of theory was chosen since it has been previously confirmed to well reproduce the geometries and excitation energies for charged PCHs.[37] Since the doubly reduced and oxidized states do not give open-shell solution, we adopted the RB3LYP/6-311G* method. The optimized geometry of the reduced model **DIAn** and the experimentally derived solid-state structures of **1** and **2** are in excellent agreement (See SI).

Compared with the neutral state, the singly reduced and oxidized states similarly exhibit smaller bond-length alternation at the core anthracene moiety, while the doubly reduced and oxidized states exhibit much smaller one. These computational results also justify their resonance structures (Figure 1) and the experimental observations discussed in the previous sections. HOMO and LUMO density plots are shown in Figures 6a and 6b, respectively. In both plots, the orbital density is largely delocalized over the 5-6-6-6-5 core of **DIAn** with some density on the outer benzenoid rings. The SOMO density plots for **DIAn**$^{\bullet+}$ and **DIAn**$^{\bullet-}$ in their doublet states are depicted in Figures 6c and 6d, respectively. At first glance there is a strong resemblance between the neutral HOMO density plot and radical cation SOMO density plot. Likewise, a similar relationship is evident between the neutral LUMO density plot and radical anion SOMO density plots. This is rationalized by recognizing that in the first oxidation process an electron is removed from the HOMO, creating a singly occupied state of approximate orbital density and symmetry. Likewise, in the first reduction process we observe a similar orbital symmetry and density between the monoanion SOMO and neutral LUMO. This is further supported by the small change in geometry from neutral **DIAn** to radical anion **1** upon reduction (Figure 5).

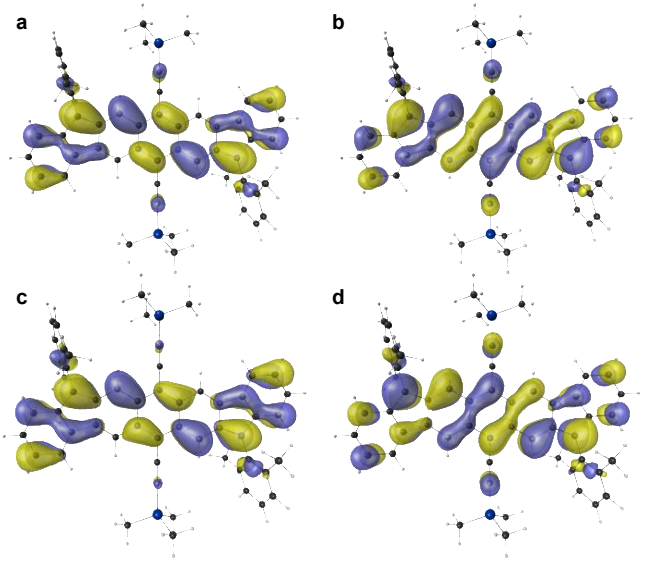

Figure 6. HOMO (a) and LUMO (b) density plots of the neutral model **DIAn** in the singlet state at the LC-RBLYP/6-311+G** level of theory. SOMO density plots for the radical cation (c) and radical anion (d) doublet states at the LC-UBLYP/6-311+G** level of theory. Each plotted at 0.02 a.u. isosurface values.

Electrostatic potential maps were calculated at the LC-UBLYP/6-311+G** on the **DIAn** model system and the two diionic states. For the neutral species we observe marginal charge on the core and substituents, as expected for a neutral species (Figure 7a). In the **DIAn**$^{2-}$ model, regions of negative charge are localized near the five-membered ring and adjacent ring on the anthracene core (Figure 7b). The central benzenoid ring and ethynyl substituents show a distinct lack of charge. Moving to **DIAn**$^{2+}$ an analogous distribution of charge is apparent with the five-membered rings containing the most electropositive regions (Figure 7c). Along with the electrostatic potential maps, a Hirshfeld charge analysis indicates that charges in both diionic states are greatest on the apical carbon atoms connecting the outer benzenoid rings and the inner anthracene. This is in excellent agreement with the solid-state structure of **3** as the K atoms are bonded in η^5- and η^6-coordination modes. An alternate explanation could be that these are also the most accessible sites on the **DIAn** core owing to the bulkiness of Si(*i*-Pr)$_3$ and Mes substituents. Nevertheless, the computational studies are in good agreement with experimental data and the redox processes outlined above.

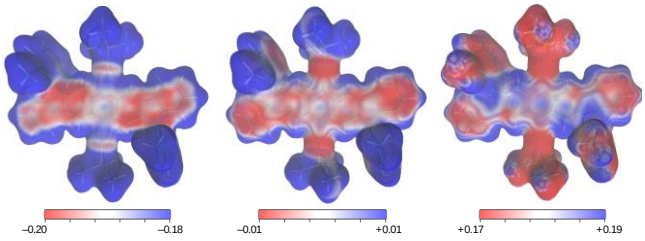

Figure 7. Electrostatic potential maps electrostatic potential maps calculated at LC-UBLYP(μ=0.33)/6-311+G** for the model **DIAn** in the dianionic (a), neutral (b), and dicationic states (c). Red (blue) region represents negative (positive) charges for **a**, more (less) negative charges for **b**, and more (less) positive charges for **c**.

Conclusions

We have shown that **DIAn** is a cyclopenta-fused PCH that can accept or donate electrons reversibly with charges primarily localized on the five-membered rings.

As a result of the biradical character and the resonance relationship between quinoidal (acceptor) and aromatic (donor) structures in the ground state, **DIAn** is able to stabilize both negative and positive charges. Through spectroelectrochemical experiments we identified low energy absorptions (ca. 0.7 eV) in the monoradical states and assigned these transitions to HOMO→SOMO for **DIAn**$^{\bullet-}$ and SOMO→LUMO for **DIAn**$^{\bullet+}$ by TD-DFT methods. Raman spectroscopy in conjunction with in situ electrolysis indicated that the structures of radical cation/anion and dication/dianion states are quite similar. This translates to a minimal change in geometry upon polaronic-like formation, an attractive feature for organic electronic applications as large structural reorganization typically hampers electronic performance.[38] Investigation of the non-contact crown-ether potassium salts of **DIAn**$^{\bullet-}$ and **DIAn**$^{2-}$ through single-crystal X-ray diffraction provided a clear picture of the structural consequences of successive single-electron charging. Finally, a quantum chemical computational study supported our experimental results and detailed the localization of charge on the polycyclic core. From multiple experimental and spectroscopic techniques we conclude that the cyclopenta-fused rings are the predominant sites of the rich redox chemistry observed in **DIAn**, in accord with the sites of highest odd-electron density in the ground state. This study represents a unique case where the stability of a neutral open-shell compound allows for the thorough characterization and structural analysis across four redox states. Future work will focus on tuning the solid-state packing and device performance of the diindeno[*b*,*i*]anthracene system.

ASSOCIATED CONTENT

Supporting Information

The Supporting Information is available free of charge on the ACS Publication website at DOI: 10.1021/jacs.xxxxxxx

Crystallographic data for **1**-**3** (CIF)
Experimental procedures, computational details and xyz coordinates, and copies of spectra (PDF)

AUTHOR INFORMATION

Corresponding Authors

*Email: haley@uoregon.edu
*Email: casado@uma.es
*Email: mpetrukhina@albany.edu
*Email: mnaka@cheng.es.osaka-u.ac.jp

Notes

The authors declare no competing financial interests.

ACKNOWLEDGMENT

This work was supported by the US National Science Foundation (CHE-1301485 to M.M.H., CHE-1212441 and MRI-1337594 to M.A.P.), by the Spanish Government, MINECO (CTQ2012-33733 and CTQ2011-26507), from Junta de Andalucía (P09-FQM-4708) and Generalitat Valenciana (PrometeoII/2014/076), and by Japan Society for the Promotion of Science (JSPS) KAKENHI Grant Numbers JP15J04949, JP25248007, JP24109002, JP15H00999 and JP26107004.

REFERENCES

(1) Müllen, K. *Chem. Rev.* **1984**, *84*, 603–684.
(2) Benshafrut, R.; Shabtai, E.; Rabinovitz, M.; Scott, L. T. *Eur. J. Org. Chem.* **2000**, 1091–1106.
(3) Bock, H.; Gharagozloo-Hubmann, K.; Sievert, M.; Prisner, T.; Havlas, Z. *Nature* **2000**, *404*, 267–269.
(4) Zabula, A. V.; Filatov, A. S.; Spisak, S. N.; Rogachev, A. Y.; Petrukhina, M. A. *Science* **2011**, *333*, 1008–1011.
(5) Sternfeld, T.; Rabinovitz, M. In *Carbon Rich Compounds: From Molecules to Materials*; Haley, M. M.; Tykwinski R., Eds.; Wiley-VCH: Weinheim, Germany, 2006; pp. 566–624.
(6) *Organic Redox Systems: Synthesis, Properties and Applications;* Nishinaga, T., Ed.; Wiley-VCH: New York, 2016.
(7) Huskinson, B.; Marshak, M. P.; Suh, C.; Er, S.; Gerhardt, M. R.; Galvin, C. J.; Chen, X.; Aspuru-Guzik, A.; Gordon, R. G.; Aziz, M. J. *Nature* **2014**, *505*, 195–198.
(8) Larcher, D.; Tarascon, J.-M. *Nat. Chem.* **2015**, *7*, 19–29.
(9) Abe, M. *Chem. Rev.* **2013**, *113*, 7011–7088.
(10) Zeng, Z.; Shi, X.; Chi, C.; López Navarrete, J. T.; Casado, J.; Wu, J. *Chem. Soc. Rev.* **2015**, *44*, 6578–6596.
(11) Kubo, T. *Chem. Lett.* **2015**, *44*, 111–122.
(12) Sun, Z.; Zeng, Z.; Wu, J. *Acc. Chem. Res.* **2014**, *47*, 2582–2591.
(13) Sun, Z.; Ye, Q.; Chi, C.; Wu, J. *Chem. Soc. Rev.* **2012**, *41*, 7857–7889.
(14) Nakano, M.; Kishi, R.; Nitta, T.; Kubo, T.; Nakasuji, K.; Kamada, K.; Ohta, K.; Champagne, B.; Botek, E.; Yamaguchi, K. *J. Phys. Chem. A* **2005**, *109*, 885–891.
(15) Motomura, S.; Nakano, M.; Fukui, H.; Yoneda, K.; Kubo, T.; Carion, R.; Champagne, B. *Phys. Chem. Chem. Phys.* **2011**, *13*, 20575–20583.
(16) Anthony, J. E.; Facchetti, A.; Henney, M.; Marder, S. R.; Zhan, X. *Adv. Mater.* **2010**, *22*, 3876–3892.
(17) Zhou, K.; Dong, H.; Zhang, H.-L.; Hu, W. *Phys. Chem. Chem. Phys.* **2014**, *16*, 22448–22457.
(18) Zhao, Y.; Guo, Y.; Liu, Y. *Adv. Mater.* **2013**, *25*, 5372–5391.
(19) Janoschka, T.; Hager, M. D.; Schubert, U. S. *Adv. Mater.* **2012**, *24*, 6397–6409.
(20) Morita, Y.; Nishida, S.; Murata, T.; Moriguchi, M.; Ueda, A.; Satoh, M.; Arifuku, K.; Sato, K.; Takui, T. *Nat. Mater.* **2011**, *10*, 947–951.
(21) Lee, J.; Lee, E.; Kim, S.; Bang, G. S.; Shultz, D. A.; Schmidt, R. D.; Forbes, M. D. E.; Lee, H. *Angew. Chem. Int. Ed.* **2011**, *50*, 4414–4418.
(22) Barnes, J. C.; Fahrenbach, A. C.; Cao, D.; Dyar, S. M.; Frasconi, M.; Giesener, M. A.; Benitez, D.; Tkatchouk, E.; Chernyashevskyy, O.; Shin, W. H.; Li, H.; Sampath, S.; Stern, C. L.; Sarjeant, A. A.; Hartlieb, K. J.; Liu, Z.; Carmieli, R.; Botros, Y. Y.; Choi, J. W.; Slawin, A. M. Z.; Ketterson, J. B.; Wasielewski, M. R.; Goddard, W. A.; Stoddart, J. F. *Science* **2013**, *339*, 429–433.
(23) Chase, D. T.; Fix, A. G.; Kang, S. J.; Rose, B. D.; Weber, C. D.; Zhong, Y.; Zakharov, L. N.; Lonergan, M. C.; Nuckolls, C.; Haley, M. M. *J. Am. Chem. Soc.* **2012**, *134*, 10349–10352.
(24) Koike, H.; Chikamatsu, M.; Azumi, R.; Tsutsumi, J.; Ogawa, K.; Yamane, W.; Nishiuchi, T.; Kubo, T.; Hasegawa, T.; Kanai, K. *Adv. Funct. Mater.* **2015**, *26*, 277–283.
(25) Kubo, T.; Shimizu, A.; Sakamoto, M.; Uruichi, M.; Yakushi, K.; Nakano, M.; Shiomi, D.; Sato, K.; Takui, T.; Morita, Y.; Nakasuji, K. *Angew. Chem. Int. Ed.* **2005**, *44*, 6564–6568.
(26) Rudebusch, G. E.; Zafra, J. L.; Jorner, K.; Fukuda, K.; Marshall, J. L.; Arrechea-Marcos, I.; Espejo, G. L.; Ortiz, R. P.; Gómez-García, C. J.; Zakharov, L. N.; Nakano, M.; Ottosson, H.; Casado, J.; Haley, M. M. *Nat. Chem.* **2016**, *8*, 753–759.

(27) Yamaguchi, K. In *Self-Consistent Field: Theory and Applications*; Carbo, R., Klobukowski, M., Eds.; Elsevier: Amsterdam, The Netherlands; 1990; pp. 727–828.

(28) Shimizu, A.; Hirao, Y.; Matsumoto, K.; Kurata, H.; Kubo, T.; Uruichi, M.; Yakushi, K. *Chem. Commun*. **2012**, *48*, 5629–5631.

(29) Dong, S.; Herng, T. S.; Gopalakrishna, T. Y.; Phan, H.; Lim, Z. L.; Hu, P.; Webster, R. D.; Ding, J.; Chi, C. *Angew. Chem. Int. Ed*. **2016**, *in press* (DOI: 10.1002/anie.201603135).

(30) Huang, R.; Phan, H.; Herng, T. S.; Hu, P.; Zeng, W.; Dong, S.-Q.; Das, S.; Shen, Y.; Ding, J.; Casanova, D.; Wu, J. *J. Am. Chem. Soc*. **2016**, *in press* (DOI: 11.10.1021/jacs.6b06188).

(31) Mondal, R.; Tönshoff, C.; Khon, D.; Neckers, D. C.; Bettinger, H. F. *J. Am. Chem. Soc.* **2009**, *131*, 14281–14289.

(32) Cataldo, F.; Iglesias-Groth, S.; Manchado, A. *Spectrochim. Acta A* **2010**, *77*, 998–1004.

(33) Ohashi, K.; Kubo, T.; Masui, T.; Yamamoto, K.; Nakasuji, K.; Takui, T.; Kai, Y.; Murata, I. *J. Am. Chem. Soc.* **1998**, *120*, 2018–2027.

(34) Zabula, A. V.; Spisak, S. N.; Filatov, A. S.; Grigoryants, V. M.; Petrukhina, M. A. *Chem. Eur. J.* **2012**, *18*, 6476–6484.

(35) Casado, J.; Miller, L. L.; Mann, K. R.; Pappenfus, T. M.; Higuchi, H.; Ortí, E.; Milián, B.; Pou-Amérigo, R.; Hernández, V.; López Navarrete, J. T. *J. Am. Chem. Soc.* **2002**, *124*, 12380–12388.

(36) Rudebusch, G. E.; Fix, A. G.; Henthorn, H. A.; Vonnegut, C. L.; Zakharov, L. N.; Haley, M. M. *Chem. Sci*. **2014**, *5*, 3627–3633.

(37) Rose, B. D.; Sumner, N. J.; Filatov, A. S.; Peters, S. J.; Zakharov, L. N.; Petrukhina, M. A.; Haley, M. M. *J. Am. Chem. Soc.* **2014**, *136*, 9181–9189.

(38) Yavuz, I.; Martin, B. N.; Park, J.; Houk, K. N. *J. Am. Chem. Soc*. **2015**, *137*, 2856–2866.